Changes of Decadal SST Variations in the Subpolar North Atlantic under Strong CO_2 Forcing as an Indicator for the Ocean Circulation's Contribution to Atlantic Multidecadal Variability

RALF HAND

Max Planck Institute for Meteorology, Hamburg, Germany, and Oeschger Centre for Climate Change Research, and Institute of Geography, University of Bern, Bern, Switzerland

JÜRGEN BADER

Max Planck Institute for Meteorology, Hamburg, Germany, and Uni Climate, Uni Research, and the Bjerknes Centre for Climate Research, Bergen, Norway

DANIELA MATEI

Max Planck Institute for Meteorology, Hamburg, Germany

ROHIT GHOSH

Max Planck Institute for Meteorology, Hamburg, Germany, and Department of Meteorology, University of Reading, Reading, United Kingdom

JOHANN H. JUNGCLAUS

Max Planck Institute for Meteorology, Hamburg, Germany

(Manuscript received 6 November 2018, in final form 13 December 2019)

ABSTRACT

The question of whether ocean dynamics are relevant for basin-scale North Atlantic decadal temperature variability is the subject of ongoing discussions. Here, we analyze a set of simulations with a single climate model consisting of a 2000-yr preindustrial control experiment, a 100-member historical ensemble, and a 100-member ensemble forced with an incremental CO_2 increase by 1% yr^{-1}. Compared to previous approaches, our setup offers the following advantages: First, the large ensemble size allows us to robustly separate internally and externally forced variability and to robustly detect statistical links between different quantities. Second, the availability of different scenarios allows us to investigate the role of the background state for drivers of the variability. We find strong evidence that ocean dynamics, particularly ocean heat transport variations, form an important contribution to generate the Atlantic multidecadal variability (AMV) in the Max Planck Institute Earth System Model (MPI-ESM). Particularly the northwest North Atlantic is substantially affected by ocean circulation for the historical and preindustrial simulations. Anomalies of the Labrador Sea deep ocean density precede a change of the Atlantic meridional overturning circulation (AMOC) and heat advection to the region south of Greenland. Under strong CO_2 forcing, the AMV–SST regression pattern shows crucial changes: SST variability in the northwestern part of the North Atlantic is strongly reduced, so that the AMV pattern in this scenario is dominated by the low-latitude branch. We found a connection to changes in the deep-water formation that cause a strong reduction of the mean AMOC and its variability. Consequently, ocean heat transport convergence becomes less important for the SST variability south of Greenland.

Supplemental information related to this paper is available at the Journals Online website: https://doi.org/10.1175/JCLI-D-18-0739.s1.

Corresponding author: Ralf Hand, ralf.hand@giub.unibe.ch

DOI: 10.1175/JCLI-D-18-0739.1

© 2020 American Meteorological Society. For information regarding reuse of this content and general copyright information, consult the AMS Copyright Policy (www.ametsoc.org/PUBSReuseLicenses).

source: https://doi.org/10.7892/boris.142262 | downloaded: 12.10.2024

1. Introduction

Atlantic multidecadal variability (AMV) is the dominant mode of sea surface temperature (SST) variability in the North Atlantic on decadal time scales (Schlesinger and Ramankutty 1994). Because the ocean's heat capacity is much higher than that of the atmosphere, a better understanding of the ocean dynamics and the pathways by which temperature anomalies in the upper ocean are communicated to the atmosphere might offer a potential to improve the predictability for the North Atlantic region, particularly on decadal time scales. However, the mechanisms that generate the AMV are only poorly understood and the subject of ongoing discussions.

One point of view is that the AMV might be a response to variability in the surface turbulent heat fluxes into the ocean. Recent studies attribute the AMV modulation to changes in the atmospheric aerosol concentration, either volcanic (Otterå et al. 2010) or anthropogenic (e.g., Booth et al. 2012; Bellomo et al. 2018). Bellomo et al. (2018) suggested that external radiative forcing can explain a significant part of the AMV in the climate model CESM, basing their argumentation on the high correlation between the mean of a large ensemble of simulations and observations. Their conclusions are questioned by Kim et al. (2018), who showed that the high correlations were mainly related to the (global warming related) trend from the 1990s onward that was not fully removed when applying a linear detrending. Because of different heat capacities of the atmosphere and the ocean, the low-frequency component of the atmospheric forcing may be emphasized in the ocean (Hasselmann 1976; Frankignoul and Hasselmann 1977). This perception has been recently supported by Clement et al. (2015), who argue that they are able to simulate an AMV-like variability in a mixed layer setup with prescribed climatological ocean heat transport convergences. This experimental setup implies an absence of ocean circulation changes and hence does not allow anything other than local atmosphere–ocean fluxes controlling local mixed layer (including sea surface) temperature.

The alternative view is that ocean dynamics are generating large-scale ocean temperature anomalies through changes in the overturning and gyre heat transport convergence (e.g., Zhang and Zhang 2015; Delworth et al. 2017; Latif et al. 2004; Delworth and Mann 2000; O'Reilly et al. 2016). Based on observations of the spatiotemporal evolution of the temperature and salinity fields, Hodson et al. (2014) conclude a combination of atmospheric and oceanic processes to be the most likely cause for the North Atlantic cooling in the 1960s, rather than atmospheric drivers alone. A comment (Zhang et al. 2016) and a response paper (O'Reilly et al. 2016) question the relevance of the mixed layer experiments by Clement et al. (2015), pointing out that the sign of the turbulent heat fluxes at the ocean–atmosphere interface in the respective experiment is opposite to what is found in observations (see also Gulev et al. 2013) and in coupled ocean–atmosphere models. The authors argue that upward heat fluxes connected to warm SST anomalies are an indication that, in a "realistic" setup, the ocean contributes to the AMV.[1] In this context, it is a limitation for understanding climate variability on decadal time scales that available ocean observations are still far from being sufficient: While data coverage at the sea surface is at least satisfactory since the middle of the nineteenth century because of ship measurements (e.g., HadISST; Rayner et al. 2003), direct observations for the three-dimensional structure of the ocean are available only for a bit more than a decade. The RAPID array provides a continuous monitoring of the AMOC at 26.5°N since 2004 but has the disadvantage of providing only data at one specific latitude (Smeed et al. 2014). The Overturning in the Subpolar North Atlantic Program (OSNAP) array provides another section farther to the north, but the time series is much shorter (since 2014; Li et al. 2017). Since 2000, Argo floats provide three-dimensional measurements of different ocean variables for the upper ocean up to a depth of 2000 m (Argo 2000). Paleodata allow longer reconstructions of the ocean state variables (e.g., Hetzinger et al. 2008; Svendsen et al. 2014), but because the proxies are only available for very few locations, these suffer from large uncertainties. For this reason, until now simulations with coupled climate models have been used as a tool to understand decadal variability of the North Atlantic. It is a limitation that large differences exist among the models concerning the temporal and spatial properties of the AMV and the AMOC (Ba et al. 2014), and even recent models suffer from large biases in the mean state (IPCC 2013, Fig. 9.2.b) that also have an influence on the low-frequency variability modes (Drews and Greatbatch 2016). Strong differences occur in the amplitude of simulated AMOC variability among CMIP3 and CMIP5 models, and the correlation between the AMOC and North Atlantic surface quantities like SST, upper-ocean heat content, and surface fluxes as well as that with hemisphere-scale surface air temperature depends on the AMOC amplitude (Yan et al. 2018). Models with

[1] This conclusion is questioned by Cane et al. (2017), who argue that the sign of the turbulent surface heat fluxes may be only a result of frequency filtering.

high AMOC variability show higher predictability on decadal time scales.

Nevertheless, many models agree on the point that AMOC and North Atlantic Subpolar Gyre (SPG) variability have a low-frequency component on (multi-) decadal and longer time scales (Ba et al. 2014), which potentially induces significant ocean heat transport convergence variations that may dominate the role of local atmosphere–ocean fluxes on decadal and longer time scales.

A continuative question is how much changes in the ocean circulation mean state and/or variability under climate change are expressed in the ocean surface state variables and how do they influence the linkage between particular processes. Analyzing the differences in the coupled ocean–atmosphere system under different boundary conditions—as we will do in this paper—therefore may help to improve knowledge about these processes in an otherwise unchanged, physically consistent model framework. The majority of coupled climate models shows a substantial weakening of the meridional overturning in a warming climate (IPCC 2013, chapter 12.4.7.2), which was recently confirmed for the second half of the twentieth century by a study that uses the SST signature of the AMOC (Caesar et al. 2018). In a set of sensitivity experiments with a subset of the CMIP models, Gregory et al. (2005) found that AMOC decline is caused rather by the weaker surface heat fluxes than by changes in the freshwater fluxes. However, the exact mechanisms of what controls the AMOC and its variability are still poorly understood and therefore not consistently represented in current climate models. Reintges et al. (2017) show that the AMOC uncertainties in future climate projections of the CMIP3 and CMIP5 runs are mainly caused by model uncertainty, rather than by uncertainties in the forcing or internal variability.

Beyond the changes in the mean state, changes in AMOC variability might occur in a warming climate. Drijfhout et al. (2010) show that projected future changes of the internal variability of the AMOC can be linked to the turbulent heat flux variability in the regions of ocean convection. In their experiments the locations of the convection regions move poleward in a warming climate, going along with a northward shift of the latitude with maximum AMOC variability, while total AMOC variability becomes weaker. The results imply that AMOC variability in future climate projections might heavily suffer from the issue that convection regions are often in the wrong location in current coupled climate models (e.g., Fig. 8 in Ba et al. 2014).

The objective of this study is to investigate the statistical link between different indices of decadal climate variability in the MPI Earth System Model (MPI-ESM) and to find physical explanations for them. A starting point is a study by Tandon and Kushner (2015) that found a correlation between the AMOC and the AMV, analyzing multimodel data from CMIP5, as well as a 29-member ensemble of historical simulations (covering the period from 1920 to 2005) using CESM. Using ensemble simulations from another model (MPI-ESM) that also shows this link, we want to understand the mechanisms behind this, augmenting the view by increasing the ensemble size for higher statistical robustness and by adding a second ensemble with stronger radiative forcing. Our set of experiments comprises a 2000-yr preindustrial control run, and two 100-member ensembles: one that is forced by historical radiative forcing and another forced by a 1% CO_2 increase per year. We will show that a weakening of the links between several indices of climate variability under strong CO_2 forcing provides evidence that ocean circulation is involved in multidecadal upper-ocean temperature variability under current climate conditions, but might become less important in a warmer climate.

Particularly, we want to address the following questions:

- Does the ocean have a relevant role in driving decadal SST variability in our coupled ocean–atmosphere model? Particularly, do changes in ocean dynamics and related changes in ocean heat transport play a role?
- Does the relationship between decadal SST variability and other ocean indices change under strong CO_2 forcing?

2. Models and methods

a. MPI-ESM

The model used in this study is the Earth system model of the Max Planck Institute for Meteorology in its low-resolution version (MPI-ESM1.1-LR; Giorgetta et al. 2013). Its ocean component MPIOM (Marsland et al. 2003) is computed on a curvilinear bipolar grid with poles over Antarctica and Greenland, avoiding singularities and providing a grid refinement in the oceanic convection regions. The nominal resolution of the grid is 1.5° in the horizontal and 40 levels in the vertical dimension. The atmospheric component ECHAM6 (Stevens et al. 2013) has a spectral resolution of T63 (~1.875°) at 47 vertical levels up to 0.01 hPa. The land surface component JSBACH provides the atmospheric boundary conditions over land, accounting for changes in land use and vegetation. Ocean and atmosphere are coupled through the OASIS coupler.

b. The MPI Grand Ensemble

The MPI Grand Ensemble is a set of (ensemble) simulations with two different radiative forcings. Here we

only provide a very brief description of the experimental setup, for further details refer to the MPI Grand Ensemble reference paper (Maher et al. 2019).[2] For this study we use a subset of the MPI Grand Ensemble, including the following three types of simulations:

The first run is a *preindustrial control run* that covers 2000 years and was forced with climatological radiative forcings, including greenhouse gas concentrations, aerosols, and incoming solar radiation. The other simulations are two 100-member ensembles: The *historical ensemble* covers the period from 1850 to 2005 and was forced with historical (observed) radiative forcing. The *ensemble with strong CO_2* forcing covers 150 years. The radiative forcings of this ensemble are equivalent to those of the preindustrial control run (i.e., climatologies of the preindustrial era), except for CO_2. The CO_2 concentration starts at preindustrial conditions and then increases by 1% yr^{-1}, which results in a CO_2 doubling after about half the run and a CO_2 quadruplication by the end of the run. Both ensembles were branched from different time instances of the preindustrial control simulation, with a gap of 24 years between the individual runs. Note that this does not inhibit the risk of aliasing effects, in the case of 24 years matching the period of any climate mode that affects the region of interest. We assume that this is not the case in our setup, because the time period chosen is beyond the typical time scales of atmospheric variability and we could not find any distinct peak in the power spectrum of AMOC variability/AMV in the preindustrial control simulation. The initialization was done from the same time instance of the preindustrial control run for both ensembles, so that each run in the ensemble with the strong CO_2 forcing has a counterpart in the historical ensemble that starts from the same initial conditions. For most of the analysis of the ensemble with the strong CO_2 forcing, we only used the last 50 years to allow the runs to diverge from the historical ensemble.

c. Definition of the climate indices used in this study

In our analysis we use several indices to describe decadal climate variability in the North Atlantic region. This section provides a brief description of how they were defined. The regions that are used to compute the indices are marked in Figs. 1c and 1d. Note also the statements on frequency filtering and detrending at the end of the paragraph.

The *AMV* is computed as the 10-yr low-pass-filtered area-weighted-averaged anomaly of SST in the region between the equator and 60°N and between 85°W and 0°. Furthermore, we used another SST index that we call *northwest North Atlantic SST*. It is based on a more confined region south of Greenland, that is, 50°–25°W, 45°–60°N (i.e., the black box in Fig. 1c). We consider this region separately, because it is, as we will show later, a key region for the AMV signal in the historical ensemble and the preindustrial control run, but will undergo crucial changes under strong CO_2 forcing. As a measure for the *AMOC* we used the overturning streamfunction. When showing the correlations, we refer to the time series at 45°N in 1000-m depth, a definition that was previously used in Boulton et al. (2014) and in good approximation agrees with the definition used in Ba et al. (2014). We define the *Subpolar Gyre strength* as the minimum of the barotropic streamfunction within the region between 65° and 15°W and between 50° and 65°N (i.e., the orange box in Fig. 1c). Positive values indicate a stronger Subpolar Gyre (i.e., we multiplied the barotropic streamfunction by −1). The *surface turbulent heat flux* is the sum of latent and sensitive heat fluxes with positive sign indicating upward fluxes, that is, fluxes from the ocean to the atmosphere. When using the term Labrador Sea turbulent heat fluxes, we refer to the spatial (weighted) average over the region between 60° and 40°W and between 50° and 60°N (i.e., the blue box in 65° Fig. 1c). The *Labrador Sea deep ocean density* is the three-dimensionally averaged potential density (with respect to a reference depth of 2000 m) in the same region between 1500- and 3000-m water depth. The two levels defining the Labrador Sea deep ocean density might occur rather deep when considering the observed Labrador Sea mixed layer depth, but as we will show later mixed layer depth reaches more than 2000 m in our model. The *ocean heat supply* is a simplified estimate of the ocean heat budget (previously used in, e.g., Drews and Greatbatch 2017). The computation starts from the ocean heat content as the potential temperature vertically integrated over the entire water column. The ocean heat content is then spatially integrated over the northwest North Atlantic (see definition above) and then the time derivative of this quantity is computed as centered differences in time. After that, the total radiative and turbulent heat flux integrated over the ocean surface of the same box is subtracted. For continuity the residual (i.e., the ocean heat supply) has to be heat that is transported into the box by heat advection by the ocean. Note that it is not possible to make any statements on where exactly the heat is advected from. The *ocean meridional heat transport* at a certain latitude was defined as follows (e.g., Eden and Jung 2001):

$$\mathrm{OHT}_{\mathrm{total}} = \int_{\mathrm{basin\,width}} \int_{\mathrm{bottom}}^{0} \theta v \, dx \, dz \,, \qquad (1)$$

[2] The MPI Grand Ensemble is publicly available, see https://www.mpimet.mpg.de/en/grand-ensemble/ for details.

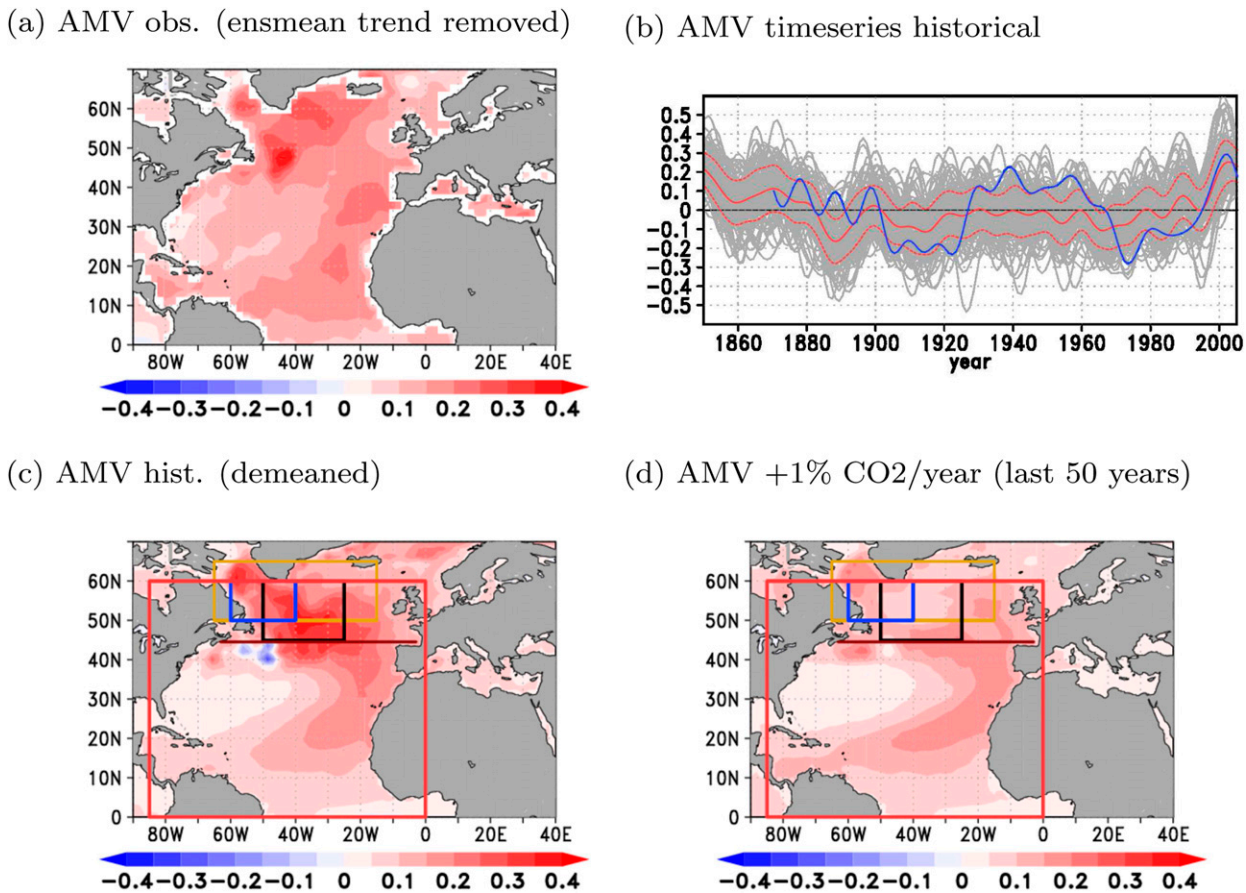

FIG. 1. Spatial structure and time series of the AMV in observations and the historical ensemble. (a) Regression of the SST on the normalized field average (85°W–0°, 0°–60°N) of SST (K per standard deviation) in HadISST. (b) AMV time series for observations (HadISST; blue), the ensemble mean of the historical ensemble (solid red) and ±1 ensemble standard deviation (dashed red) and the individual ensemble members of the historical ensemble (gray). (c) As in (a), but for the demeaned historical ensemble. (d) As in (a), but for the demeaned ensemble with an incremental CO_2 increase by +1% yr^{-1}. For (a) and (b), SSTs were detrended by removing a linear fit to the ensemble mean SST of the historical ensemble. In (c) and (d), the ensemble mean itself was removed (see section 2d for details). For all panels a 10-yr low-pass filter was applied. The rectangular boxes in (c) and (d) indicate the regions for computing the spatially averaged climate indices used in the following: the AMV region (red; 85°W–0°, 0°–60°N), the Labrador Sea convection region (blue; 60°–40°W, 50°–60°N), the northwest North Atlantic (black; 50°–25°W, 45°–60°N), and the Subpolar Gyre region (orange; 65°–15°W, 50°–65°N). The brown line indicates the latitude of our AMOC index.

where θ is the potential temperature and v the meridional velocity,

$$\mathrm{OHT}_{\mathrm{moc}} = \int_{\text{basin width}} \int_{\text{bottom}}^{0} \overline{\theta}\,\overline{v}\,dx\,dz, \tag{2}$$

where the overbars denote the zonal mean of θ and v, and

$$\mathrm{OHT}_{\mathrm{gyre}} = \int_{\text{basin width}} \int_{\text{bottom}}^{0} \theta' v'\,dx\,dz, \tag{3}$$

where primes denote deviations of θ and v from the zonal mean. The *overflow waters* are defined as the integrated volume transport of subsurface water crossing the Greenland–Scotland Ridge (marked by the colored lines in Fig. 4b) in a southward direction. Because the density of the deepest water crossing the ridge shows relevant changes in the simulation with strong CO_2 increase, we decided to deviate from the common criterion that considers all waters denser than 1027.8 kg m^{-3} as overflows. Instead, we use a fixed-depth criterion and integrate over all values below 100-m depth. On decadal time scales, this index shows a correlation of 0.88–0.92 with the conventional definition of the overflows in the ensemble of the historical simulations.

d. Detrending and demeaning

Within this study, we use different methods of detrending the data. On the first view it might appear a bit confusing not to limit detrending to one method throughout the

paper, but each method has its advantage, which we describe in the following.

The preindustrial control simulation by setup should not have any trend if the model is in perfect equilibrium state. We could not find any obvious drift for our simulation. Even though we removed a linear fit to account for model drift.

The second method was only applied to observations and the members of the historical ensembles. Here, we removed the linear trend of the ensemble mean of the historical ensemble from each ensemble member/the observations. The purpose of this detrending method is to remove the part of the signal that is due to the accumulation of anthropogenic greenhouse gas (GHG) emissions. The procedure keeps any variability in the radiative forcing that is different from a monotonous increase, for example, variations in natural or anthropogenic aerosols. Using this method allows us, for instance, to compare to previous studies (e.g., Bellomo et al. 2018) that quantified the direct surface-heat-flux-related effects of temporal (decadal) variations in the radiative forcing on SST (excluding the role of an interactive ocean circulation). When we refer to the externally forced signal in the linearly detrended data, these decadal variations are meant, neglecting the long-term trend (which is also externally forced).

The disadvantage of the previous method is that it would clearly be not sufficient to fully remove the strongly nonlinear trend in the run with the strong CO_2 forcing and any correlation analysis that we will show in the following, would be dominated by the residual trend. Therefore, for most of the analysis of the internal variability in the ensemble simulations we use another method that was previously used (e.g., Tandon and Kushner 2015) and is often referred to as ''demeaning.'' In this case the detrending is done by removing the ensemble mean, which, in case of a sufficiently large ensemble, represents the part of the signal that is common in all ensemble members and therefore can be directly attributed to the variations in the forcing. An advantage of the demeaning is that it does not require any a priori information on the shape of the forced signal. Note that demeaning the data removes not only the externally forced trend but also any direct response to the external forcing (which might be undesirable in some cases, as mentioned in the previous paragraph). However, the residual might still exhibit indirect effects, for example, due to triggering of certain variables.

In general, we followed a fixed processing order to compute the indices, starting from yearly 2D or 3D data, then doing the detrending by one of the two methods described in the following section, then selecting the region and computing the spatial means/integrals as appropriate and ending with application of a 10-yr Butterworth low-pass filter. An exception from this order is made for the Subpolar Gyre strength where the detrending (see section 2d) was made after computing the field minimum of the barotropic streamfunction and the ocean heat transport where the demeaning was done after computing the ocean heat transport and its components from v and θ.

e. *Computation of the measures for the internal variability and for the externally forced signals*

For large ensembles it is possible to disentangle climate variability into a part that is related to the (time varying) external forcing and a part related to internal variability. Assuming that the ensemble members are independent from each other in terms of the phase of the internal variability, the latter is averaged out in the ensemble mean. The ensemble mean therefore reflects the externally forced part of the climate signal. In contrast, the deviations of the individual runs from the ensemble mean are caused by internal variability. If the ensemble is large enough, they reflect in good approximation the possible climate states the model can capture under the external forcing at each time step. In this paper we use one ensemble standard deviation as a measure for the typical internal variability. Because we compute the standard deviation in the ensemble dimension, this method also offers the chance to detect changes of internal variability over time.

We computed the fraction of low-frequency variability that can be explained by the external forcing by dividing the time variance of 10-yr-low-pass-filtered ensemble mean time series by the ensemble average of the time variances of the 10-yr-low-pass-filtered time series computed for each ensemble member individually.

f. *Lag correlations and significance testing*

In the results section of this paper, we show lead–lag correlation analysis of the indices described in section 2c. To increase the sample size, we concatenate all runs of each ensemble instead of computing correlations for each run individually. For a detailed mathematical description, refer to the appendix.

To test these correlations for statistical significance, we used a Monte Carlo approach benefiting from the large ensemble size. We created 500 surrogates, each consisting of 100 demeaned time series of randomly chosen (with replacement) ensemble members of the original ensemble. These were concatenated in the same way as when computing the correlations for the original ensemble. The surrogates were created for each quantity

separately and then (lag) correlations between different quantities were computed accordingly. Any remaining correlation that comes out from this computation should be arbitrary, that is, without any physical meaning, because the time series of the individual quantities of each pair of surrogates usually stem from different ensemble members of the original ensembles. From these 500 correlations we estimate the quantiles of a distribution of spurious correlations between time series with the same statistical properties as the original ensemble. Note that these quantiles are very close to zero for all indices, indicating that it is very unlikely to get spurious correlation given the large size of the samples given by the Grand Ensemble.

3. Results

a. Preindustrial and historical simulations

First, we analyze decadal SST variability with climatological and historical external forcing, that is, in the preindustrial control simulation and the historical ensemble. The AMV time series (Fig. 1b) has an externally forced signal (the ensemble mean is different from zero) that shows similarities to observations, with declines in the 1900s and 1960s and increases around 1920 and 2000 (a slightly modified version of this plot, highlighting the similarity by using a different scaling, can be found in Fig. S1 in the online supplemental material; correlation of 0.54 for the period after 1900). However, the externally forced signal is rather small compared to the internal variability of the AMV in our model: only about 1/3 (36.8%) of the AMV is externally forced in the historical ensemble. Consistent with previous studies (Terray 2012) the fraction of the externally forced signal in low-frequency SST variability grid point by grid point (Fig. S1) shows that a high explained variance can be found in the low latitudes, while in the higher latitudes the direct effect of the external forcing on SST is rather small. It has to be mentioned that other models in some regions have much higher sensitivity to the external forcing (Bellomo et al. 2018; Murphy et al. 2017).

The modeled SST pattern (Fig. 1c and Figs. S3a,b) is very similar to the observed AMV pattern with a horseshoe-like structure, extending from the northern North Atlantic along the eastern Atlantic toward the tropics. The absolute maximum of variability is located in the northwest North Atlantic. However, compared to the observed AMV pattern this maximum is somewhat larger and extends farther to the east. We hypothesize that this might be a consequence of a bias in the path of the North Atlantic Current in the model (Jungclaus et al. 2013). The latter is too zonal in our model, which alters the transport pathways of subtropical water masses into the northern North Atlantic. Furthermore, SST variability in the low-latitude branch is slightly underestimated and the model shows a local minimum with negative regression coefficients in the Gulf Stream extension region that cannot be found in observations. The modeled pattern shows only little difference between the preindustrial control simulation and the historical ensemble (pattern correlation of 0.92 for the domain of Figs. S3a and S3b), indicating that the existence of a time-varying external forcing does not play an important role for the AMV pattern in the historical period in our model. As in observations, the spatiotemporal evolution of the AMV pattern (Fig. S4) shows a warming in the Gulf Stream region several years before the AMV index peaks. The warming occurs earlier in observations than in the model. In the model the Gulf Stream region shows negative SST anomalies after the AMV peak that cannot be found in observations.

In the following, we will focus on the northwestern part of the North Atlantic between 50° and 25°W and between 45° and 60°N (i.e., the black box in Fig. 1c). Three reasons exist to focus on this region: 1) It shows the highest regression coefficients when regressing the AMV index on the decadally filtered 2D SST field in the preindustrial run and the historical ensemble. 2) As we will show later, these high regression coefficients will decrease under strong CO_2 forcing. 3) Upper-ocean temperature variability is strongly related to the AMOC in this region, particularly on decadal time scales (Fig. S6). To understand what influences decadal-scale SST variability in this region, we computed lead–lag correlations with different climate indices for the North Atlantic region. SST in this region has a very strong in-phase correlation with the AMV index (red line in Fig. 2c and Fig. S7). The correlation between northwest Atlantic SST and upward turbulent heat flux in the same region is positive (black lines in Fig. 2c and Fig. S7). This means that warm SST anomalies are associated with heat loss from the ocean to the atmosphere, indicating that the SST is not driven by surface turbulent and latent heat fluxes. While Cane et al. (2017) point to possible flaws with this conclusion, we can clearly show that ocean dynamics play a role in our model: The ocean heat supply (for a brief description refer to section 2c) in the northwest North Atlantic (50°–25°W, 45°–60°N) is strongly correlated with the decadal component of SST variability in the northwest North Atlantic (correlation coefficient of 0.8 at lag 0). Even when using unfiltered yearly mean data, there is a correlation of

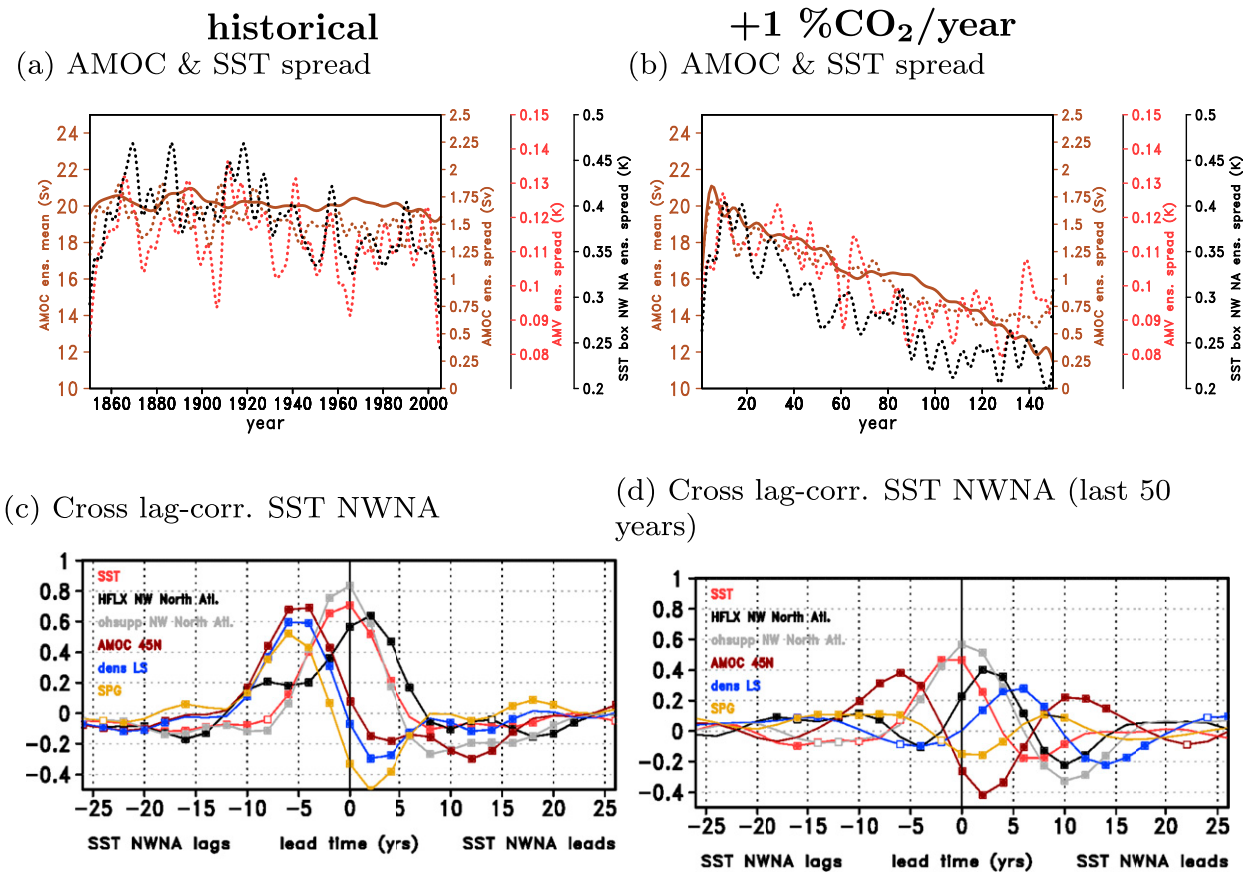

FIG. 2. (a),(b) AMOC at 45°N (brown) mean (solid) and ensemble spread (dotted) and ensemble spread of the AMV (red, dotted) and the northwest North Atlantic SST (black, dotted) in the historical ensemble in (a) and the last 50 years of the ensemble with an incremental CO_2 increase by +1% yr^{-1} in (b). Time series are undetrended and 10-yr low-pass filtered. (c),(d) Lag correlation of the SST in the northwest North Atlantic with the AMV index (red; defined as in Fig. 1), with the ocean–atmosphere turbulent heat flux in the northwest North Atlantic region (black; positive upward), the ocean heat supply as the residual between the ocean heat content change integrated over the northwest North Atlantic region minus the turbulent flux to the atmosphere over the same region (gray), the AMOC (as the overturning streamfunction at 1000-m depth) at 45°N (brown), the potential density (w.r.t. 2000 m) averaged for the deep ocean in the Labrador Sea convection region (60°–40°W, 50°–60°N; 1500–3000-m depth), and the Subpolar Gyre strength (orange) as the field mean of the barotropic streamfunction in the SPG region multiplied by −1 to get positive values for a stronger SPG in the historical ensemble in (c) and the ensemble with an incremental CO_2 increase by +1% yr^{-1} in (d). In (c) and (d), nonfilled (filled) markers indicate significance at the 98% (99%) confidence level based on the test described in section 2f, detrended by removing the ensemble mean of each quantity and 10-yr low-pass-filtered.

0.6 between ocean heat supply and northwest North Atlantic SST (Fig. S8).[3] As mentioned before, the definition of the ocean heat supply does not allow us to locate the source of the oceanic heat advection. However, we found that also the AMOC at 45°N has a very high correlation with the SST box mean, with a maximum correlation coefficient of 0.7 on decadal time scales (0.5 on annual time scales) when the AMOC leads by ~5 years. The same holds for the AMOC at 26°N (not shown) with a shorter lag for the maximum correlation (indicating a southward propagation of the AMOC intensification) and slightly lower correlation coefficients ($r = 0.6$ at lag 0). To test the robustness of the correlations between the AMOC and the northwest North Atlantic SST, we computed correlations for each ensemble member of the historical ensemble separately (gray lines in Fig. S9a). There is a spread in the correlations, but the strong positive correlation around a lag of ~4 years also holds for the individual ensemble members, indicating robustness of this result. Another strong link is found to Labrador Sea deep ocean density that integrates signals from local

[3] We verified that this correlation is caused by AMV-related SST variability by splitting the SST variability into an AMV and a non-AMV part and recomputing the correlation for each of these two separately.

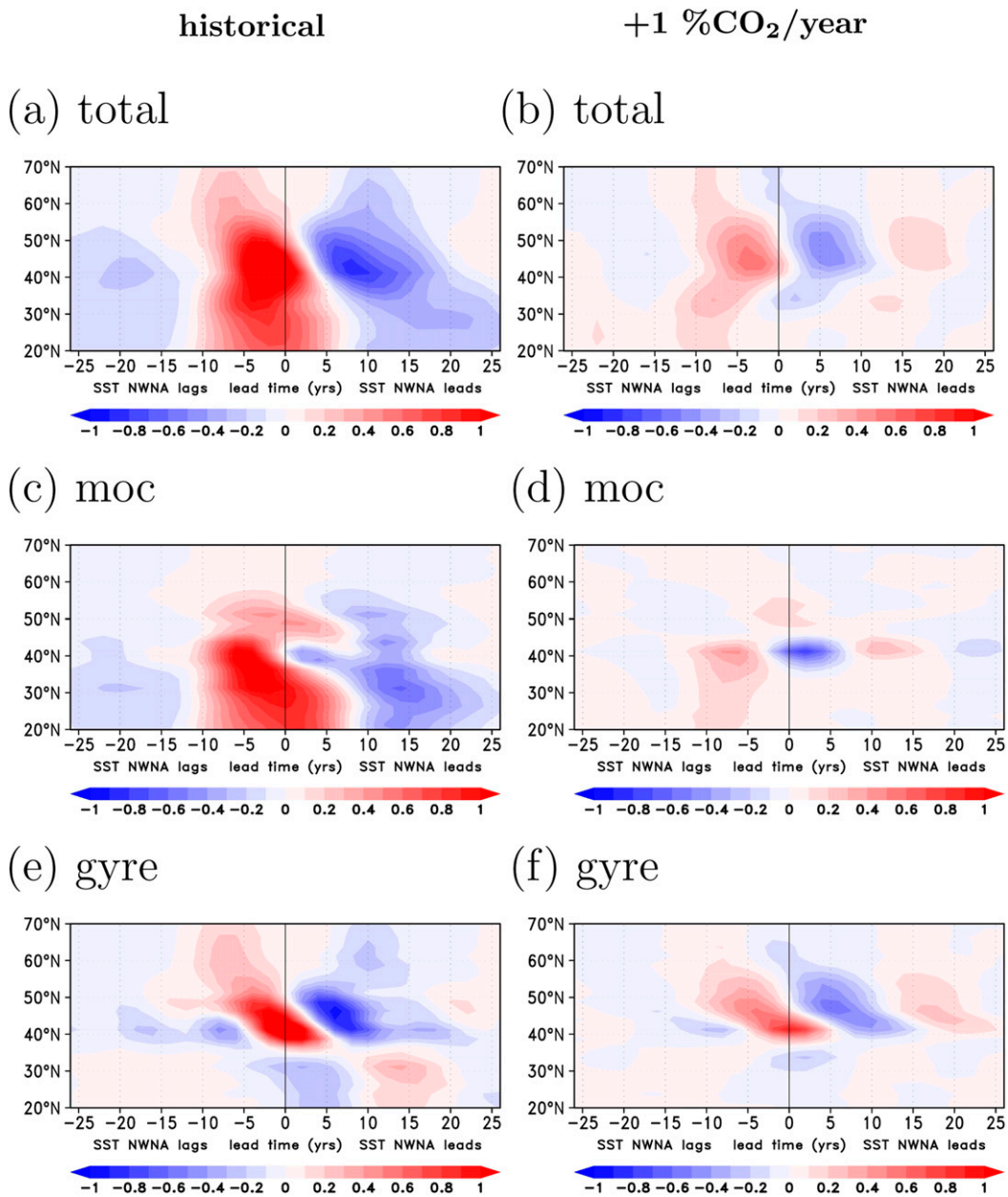

FIG. 3. Regression of the convergence of northward ocean heat transport in the Atlantic on the SST box mean in the northwest North Atlantic (10^8 W m^{-1} per standard deviation of the northwest North Atlantic SST index) in the (left) historical ensemble and (right) ensemble with an incremental SST increase by +1% CO_2 yr^{-1} for the (a),(b) total ocean heat transport and separated for the (c),(d) overturning and (e),(f) gyre heat transport. All data were 10-yr low-pass filtered and the trend/external signal was removed by subtracting the ensemble means.

convection and the overflows. Deep densities in the Labrador Sea region modulate the density gradients driving the MOC (Lozier et al. 2010). The correlation between density variability and northwest North Atlantic SST has a maximum correlation coefficient of 0.6 when density is leading the SST by ~4–6 years (Fig. 2c).

The left column of Fig. 3 shows the meridional derivative of northward ocean heat transport [total (Fig. 3a) and separated for the overturning (Fig. 3c) and the gyre component (Fig. 3e); for details see section 2c] regressed on the SST index for the northwest North Atlantic for the historical ensemble. We define positive (negative) values indicating a heat transport convergence (divergence) in the zonal band along at a certain latitude. For about 10 years before the SST index peaks, there is heat transport convergence in the entire midlatitude North

Atlantic. This is mainly caused by the oceanic overturning that accumulates heat mainly in the region south of about 45°N. Between about 38° and 50°N the gyre plays an important role in transporting heat northward in the last ~6 years before the SST peaks. The signal in the gyre component starts at high latitudes and then propagates southward. In this context we would like to mention that the overturning and gyre circulation should not be seen as processes that are independent from each other, since previous studies showed a dynamic coupling between these two (Yeager 2015; Oldenburg et al. 2018).

Figure 2a shows the undetrended ensemble mean AMOC at 45°N, and the ensemble spread of the low-pass-filtered AMOC, AMV, and northwest North Atlantic SST throughout the historical period. The ensemble mean AMOC varies between 19 and 22 Sverdrups (Sv; $1\,\mathrm{Sv} \equiv 10^6\,\mathrm{m^3\,s^{-1}}$) without any obvious trend. There are year-to-year variations in the ensemble spread (1.25–2 Sv) that are likely a residual from not fully averaging out internal variability, but also might include changes in external variability triggered due to the external forcing. These variations are small compared to the AMOC's mean value and in the order of magnitude of the time standard deviation of the individual runs (which ranges from 1.2 to 4 Sv). AMV and northwest North Atlantic SST spread vary consistently, underlining the important role of the northwest North Atlantic in the AMV signal. The ensemble spread of the temperature indices shows weak indication for a decline toward the end of the historical runs; however, this trend is small compared to the year-to-year variability.

As shown before, Labrador Sea deep ocean density shows a strong statistical link to northwest North Atlantic SST. The Labrador Sea forms (beside the central Nordic Sea) one of the two main northern convection regions in our model in the preindustrial control experiment (not shown) and in the historical ensemble (Fig. 4a). Figure 4c shows lag cross correlations between the deep ocean (1500 to 3000 m water depth) density averaged over the Labrador Sea and different other ocean variables. Labrador Sea density shows a very high correlation with the AMOC at 45°N (correlation coefficient up 0.8). Decadal density variability is linked to local convection ($r_{\max} = 0.6$ when local convection leads by 2 years) and the Denmark Strait overflow transport ($r_{\max} = 0.45$ when the overflows lead by 2 years), while the correlation with the overflows in the eastern part of the Atlantic is small (Fig. S10).

b. *Simulations with strong CO_2 forcing*

In this section, the previous analysis is repeated, but for strong CO_2 forcing. Unless otherwise specified, this means that we analyzed the last 50 years of the run with an incremental CO_2 increase by 1% yr^{-1}. We will show that the characteristics of the AMV and the AMOC undergo crucial changes and we will provide a consistent mechanism that links these changes in deep-water properties in the Labrador Sea.

Figure 1d shows the AMV pattern as previously defined. The striking difference compared to historical/preindustrial conditions is that the maximum in the northwest North Atlantic has completely vanished, and the pattern now shows some resemblance of the pattern in the slab ocean experiment by Clement et al. (2015). The highest regression coefficients can now be found in the Labrador Sea (that also strongly regresses on AMV under historical forcing) and south of Newfoundland and the low-latitude branch is more pronounced relative to the high-latitude branch than under historical forcing. The lag cross correlations of the northwest North Atlantic (NWNA) SST show similarity to those from the historical runs for AMOC, basinwide AMV, surface turbulent heat flux, and ocean heat supply, but with strongly reduced correlation coefficients. For the link with the Subpolar Gyre strength and deep ocean potential density in the Labrador Sea, the correlations even do not show qualitative similarity, but almost completely vanish with correlation coefficients below 0.3 under strong CO_2 forcing. Figure 2b shows crucial changes in the AMOC under strong CO_2 forcing: The ensemble mean AMOC declines from ~20 Sv at the time of initialization to only about 12 Sv toward the end of the run. The decline goes along with a decline in the ensemble spread. Also for the ensemble spread of the temperature indices, the trend becomes the dominant feature compared to changes in the spread on shorter time scales.[4] The AMOC decline does not go along with a spatial shift of the overturning cell (Fig. S11). The regression of total ocean heat transport convergence on low-frequency northwest North Atlantic SST variability becomes much weaker (right column of Fig. 3). Particularly the contributions of the AMOC to North Atlantic SST variability are fundamentally different from those in the historical ensemble (Fig. 3d). The gyre contributions show a similar pattern, but with weaker regression coefficients (Fig. 3f).

As we found strong indications for a link between the northwest North Atlantic SST and the ocean circulation in the previous section, this raises the question of whether the changes in variability can also be linked to changes in ocean variability. The link to Labrador Sea deep ocean density is substantially weaker ($r \leq 0.3$).

[4] Typical time standard deviation of the AMV (northwest North Atlantic SST) in the individual runs: 0.01 (0.08) K.

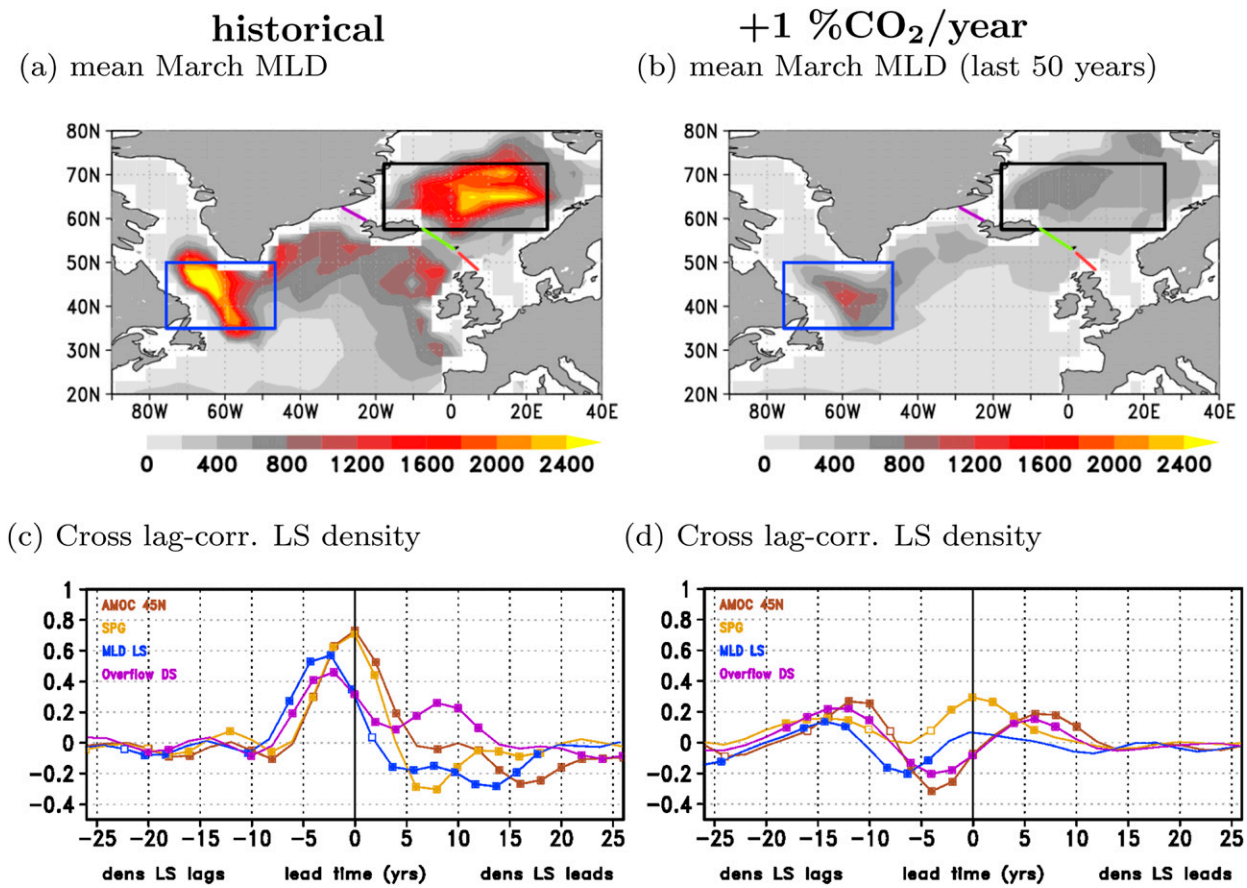

FIG. 4. (a),(b) Temporal and ensemble average of the mixed layer depth in March for the historical ensemble in (a) and the last 50 years of the ensemble with an incremental CO_2 increase by +1% yr^{-1} in (b). The blue box indicates the Labrador Sea convection region used to compute the density index in (c) and (d); the black box is what we refer to as the Nordic seas. The purple, green, and red line indicates the sections to compute the Denmark Strait, the Iceland–Faroe Ridge, and the Faroe–Scotland Ridge. (c),(d) Lag correlation of the potential density (w.r.t. 2000 m) averaged for the deep ocean in the Labrador Sea convection region (60°–40°W, 50°–60°N; 1500–3000-m depth) and the AMOC at 45°N (brown), the Subpolar Gyre strength (as previously defined, orange), the surface turbulent heat flux averaged over the Labrador Sea (blue), and the volume transport of the Denmark Strait overflow (purple). Nonfilled (filled) markers indicate significance at the 98% (99%) confidence level based on the test described in section 2f. All indices were detrended by removing the ensemble mean of each quantity and 10-yr low-pass-filtered.

Figure 4b shows the time- and ensemble-averaged 2D fields of the mixed layer depth in the northern North Atlantic. The location of the convection regions has not changed much with respect to the runs with historical forcing, but convection strength has declined drastically.

The vertical profile of the Labrador Sea potential density (Fig. 5a) changes: While the surface density becomes much lighter in the second half of the run, a layer with strong vertical gradients develops beneath in a depth between 50 and 100 m, stabilizing the water column and therefore likely suppressing deep convection in many cases. The thermal stratification of the ocean does not change very much, indicating that the stabilization is mainly by freshening. The ensemble mean properties of the Labrador Sea deep ocean density and its variability match those of the AMOC very well (Fig. 5b for absolute changes, Fig. 5c for relative changes w.r.t. the historical simulations). The internal variability of convection is more or less unchanged in the Labrador Sea for the first half of the simulations and then starts to decline in the second half, reaching about 50% of the historical value toward the end of the runs. In contrast, the convection in the Nordic seas declines earlier and the change is more abrupt.

The total overflow shows a slight decline from the middle of the simulations onward, but less distinct than the other variables (Fig. 5c). Interestingly, the variability in Denmark Strait overflow transport (which had been strongly linked to the AMOC during the historical period, see previous section and Fig. 4c) even increases for a phase in the middle of the simulation. An exact

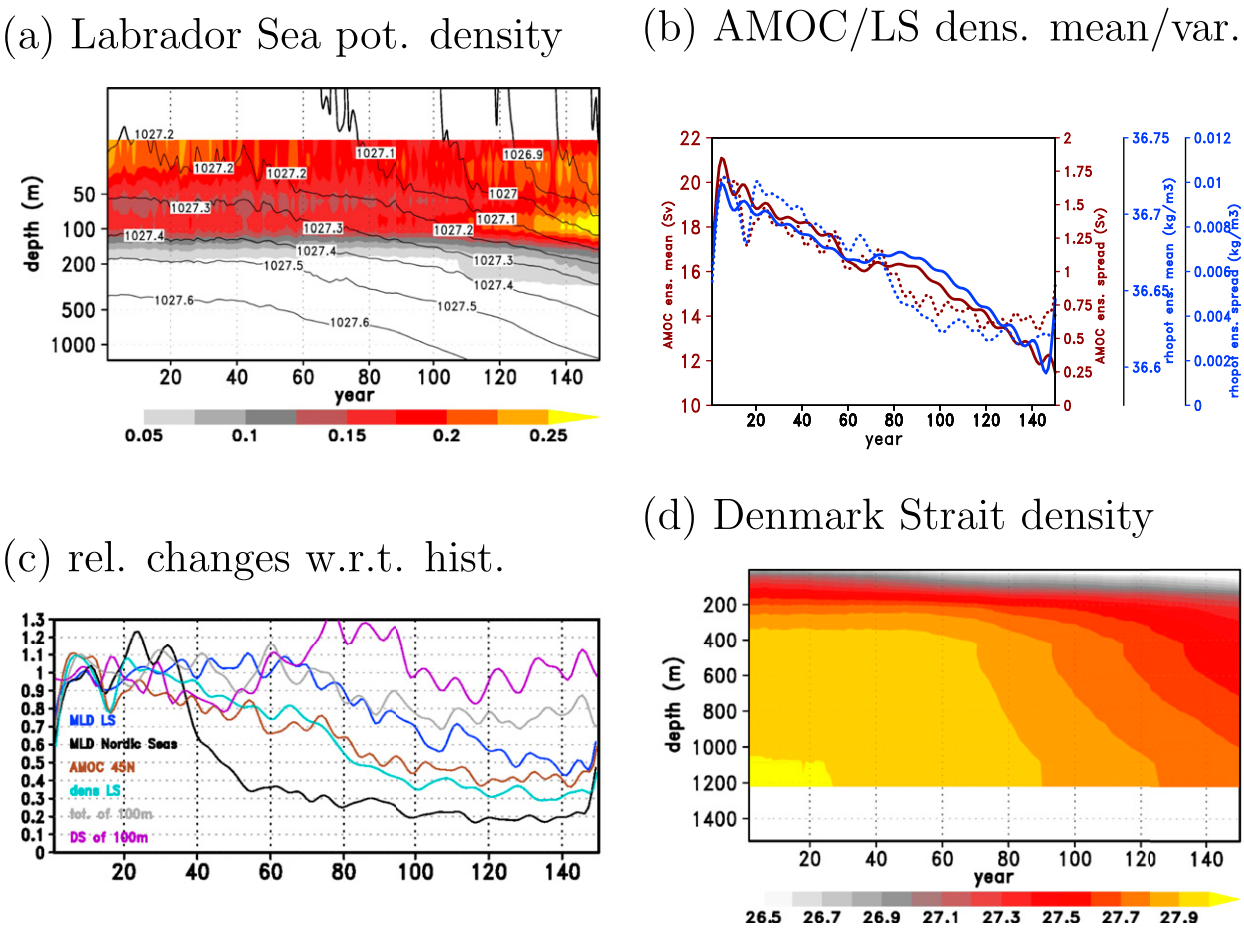

FIG. 5. Labrador Sea stratification and ocean density in the ensemble with an incremental CO_2 increase by 1% yr^{-1}. (a) Hovmöller plot of the vertical profile of the vertical derivative of potential density [shadings; kg m^{-3} (100 m)$^{-1}$ with respect to the surface] in the Labrador Sea convection region (box average for a box 60°–40°W, 50°–60°N) and potential density (contours; kg m^{-3} with respect to the surface); (b) AMOC at 45°N (brown), and potential density (w.r.t. 2000 m; blue) averaged for the deep ocean in the Labrador Sea convection region (60°–40°W, 50°–60°N; 1500–3000-m depth) mean (solid) and ensemble spread (dotted). Time series are undetrended and 10-yr low-pass filtered. (c) Relative change (w.r.t. the historical ensemble) of the ensemble spread of different ocean indices, i.e., mixed layer depth in the Labrador Sea (blue) and the Nordic seas (black), the AMOC at 45°N (brown), the deep ocean density in the Labrador Sea (light blue), and the volume transport of the overflows in total (gray) and for the Denmark Strait only (purple). The time series were demeaned and 10-yr low-pass filtered. (d) Hovmöller plot of the ocean density in the ensemble with an incremental CO_2 of 1% yr^{-1} along the Denmark Strait section. Each depth was averaged separately along the section, and the time series are undetrended and unfiltered.

quantitative breakdown of the role of individual components for their contribution to deep ocean density remains challenging, because not only the ratio between the volumes of the deep waters formed in each of the regions might change, but also the densities of the water formed in each of the regions. Figure 5d shows a decline of the mean density of water passing the Denmark Strait. Corresponding figures for the eastern sections are provided in the supplemental material (Fig. S12).

A detailed analysis of the atmospheric effects arising from the changes in SST variability is beyond the scope of this study. Here, we will only briefly show the changes in the large-scale atmospheric circulation and its variability; also, these may help to explain the changes in the ocean circulation. The mean state of the atmospheric circulation changes toward a positive NAO state (not shown), but we could not find any substantial changes to the leading large-scale atmospheric circulation variability patterns (Fig. S13). Because Figs. 3e and 3f also show some changes in the gyre-related component of the ocean heat transport convergence associated with the northwest North Atlantic SST, we additionally analyzed the internal variability of the Sverdrup transports under changed boundary conditions. However, because these show little changes under strong CO_2 forcing (Fig. S14), we see no evidence that the changes in northwest North

Atlantic variability are a consequence of wind-driven changes in the Subpolar Gyre variability.

4. Discussion

We analyzed different indices of decadal ocean variability to investigate the role of ocean circulation for upper-ocean/ocean surface temperature variability in the North Atlantic.

In contrast to findings for the CESM (Bellomo et al. 2018), the externally forced variance of decadal SST variability is small in our model. The differences between individual models might be an indication that the factors controlling decadal SST variability in certain regions might differ between models. These features may be related to differences in the sensitivity of the atmosphere or the ocean to specific components of the radiative forcing, but also particularly might include differences of (the mean state and the variability of) the ocean circulation.

We do not negate that external forcing plays a role in explaining large-scale upper-ocean temperature variability in the North Atlantic, because our historical ensemble shows a clear signal in the ensemble mean AMV. The externally forced signal of the simulated AMV correlates with observed AMV (correlation coefficient 0.54 for the period 1870–2005), indicating that the observed signal is to some extent externally forced. However, the amplitude of this signal is small compared to the internal variability of the AMV. We argue that ocean circulation is important for redistributing the heat in the ocean and for determining the spatial manifestation of the SST pattern that is associated with a basinwide defined index.

As we show, the AMV pattern in our experiments shows crucial changes under strong CO_2 forcing. While the variability in the northwest North Atlantic dominates a large part of the signal under historical and preindustrial conditions, variability in this region strongly decreases in an experiment with 1% CO_2 increase per year. Therefore, we suggest that the basinwide defined AMV index at least in our model might reflect a combination of a direct in situ response of the upper ocean to local atmospheric processes and of processes that involve the ocean circulation and related changes in ocean heat transports. In section 3a we show a strong link to Labrador Sea deep ocean density under historical forcing. Consistent with previous studies (Zhang and Zhang 2015; Drews and Greatbatch 2016; Kim et al. 2018), we suggest the following mechanism to be a driver of northwest North Atlantic decadal temperature variability in our model: A combination of anomalous salinity and surface turbulent heat fluxes drives the variability of Labrador Sea ocean convection. The local deep-water variability reflects a combination of this local convection and the intrusion of remotely produced deep water entering the subpolar basin through the Greenland–Scotland Ridge, with the waters crossing the Denmark Strait playing the most important role. As a result, positive density anomalies cause a spinup of the ocean overturning with a southward-propagating signal in the AMOC. This then leads to an anomalous transport of warm water into the northwest North Atlantic.

The reduced AMOC variability and the reduced SST variability in the northwest North Atlantic under strong CO_2 forcing are linked to the weaker forcing of forcing of deep-water formation in both convection regions. The stronger greenhouse effect leads to a warming of the atmosphere, which particularly affects the high latitudes (Arctic amplification). Under historical forcing, the colder winter temperatures in the northwest North Atlantic provide one of the main drivers of Labrador Sea convection, by causing very high surface heat loss. In case of strong CO_2 forcing, temperatures have risen, which means that these very high surface fluxes from the ocean to the atmosphere are reduced. Additionally, the forcing induces a freshening of the upper ocean. As a result of these two effects, mean ocean convection and ocean convection variability are strongly reduced. This results in lower AMOC variability and hence lower temperature variability in the northwestern North Atlantic. The basinwide-averaged SST index therefore is dominated by other regions, for example, the lower latitudes, reflected by the more pronounced low-latitude branch of the AMV pattern.

In this study we omit a detailed analysis of the atmospheric teleconnections associated with the AMV. The correlation between indices of European climate and the AMV on decadal time scales are rather small compared to internal variability in our experiments. It is a known problem that recent climate models show a large spread in terms of the simulated connection between European climate and the AMV that is inconsistent with observations for many models (Qasmi et al. 2017). A better understanding of the processes that link the North Atlantic and the European continent and an improved implementation or representation of them in the models therefore is indispensable for potential benefits that arise from our results for decadal predictions.

5. Summary and conclusions

In this paper, we analyzed the driving factors of decadal large-scale SST variability in the North Atlantic in the Max Planck Institute Grand Ensemble. Particularly, we investigated the question to what extent ocean dynamics contributes to the Atlantic multidecadal variability in

different background climates. For this purpose we analyzed a single long control simulation with climatological preindustrial radiative forcing and two 100-member ensembles of transient simulations of which one has historical forcing for the period from 1850 to 2005, and the other one has an incremental CO_2 increase by 1% yr^{-1} integrated over 150 years.

We found strong evidence that decadal SST variability in our model, particularly in the northwestern part of the North Atlantic, is mainly caused by anomalous heat supply due to variations in the ocean heat transport convergence. Under preindustrial and historical forcing we found statistically robust and physically consistent links between the density structure in the Labrador Sea, the overturning circulation, and anomalous ocean heat transport convergence. The resulting internally generated variability dominates, while the externally forced signal makes only a small part of the total decadal SST variability. The latter is in contrast to previous studies (Bellomo et al. 2018; Booth et al. 2012) and may be due to differences in the representation of indirect aerosol effects. As a concluding remark, we therefore want to encourage future model studies on the drivers of the AMV to scrutinize the role of the implementation of aerosol effects.

Under strong CO_2 forcing, the variability of all of the previously mentioned quantities declines, which is likely related to a stabilized ocean stratification in the Labrador Sea caused by enhanced vertical density gradients related to a freshening of the upper ocean. The decline in variability goes along with crucial changes in the spatial SST pattern associated with the AMV index, with the northwestern subpolar North Atlantic becoming less important, while the low-latitude North Atlantic becomes more important. We conclude that in our model, ocean circulation and related variability in ocean heat transport convergence is important to fully understand the AMV. We see the necessity to further investigate the effects resulting from (biased) transport pathways of surface water masses in the Subpolar Gyre region and related differences in the ocean–atmosphere heat and freshwater exchange.

Acknowledgments. We thank Sebastian Milinski for useful discussions and Oliver Gutjahr for the internal review of the manuscript. Furthermore, we acknowledge the constructive comments of three anonymous reviewers. The Grand Ensemble simulations were performed by Louis Kornblüh and Michael Botzet. Furthermore, we acknowledge computing time and support through the German Climate Computing Centre (DKRZ). Ralf Hand was funded by the German Federal Ministry of Education and Research (BMBF) through the project MiKlip-MOVIECLIP (Förder-Kennz. 01LP1517B). Daniela Matei was supported by the German BMBF RACE II project (FKZ.: 03F0729D) and CLIMPRE Inter-Dec (FKZ.:01LP1609A). Rohit Ghosh received funding through the European Union's Horizon 2020 research and innovation program under Grant Agreements 633211 (AtlantOS) and 727852 (Blue-Action). Scripts used in the analysis and other supplementary information that may be useful in reproducing the authors' work are archived by the Max Planck Institute for Meteorology and can be obtained by contacting publications@mpimet.mpg.de.

APPENDIX

Computation of the Correlation Coefficients for the Concatenated Ensembles

We define the correlation coefficient between time series x and y as

$$r_{xy}(\text{lag}) = \frac{\sum_{i=1}^{n}\sum_{j=1}^{m\text{-lag}}(x_{i,j}-\overline{x})(y_{i,j+\text{lag}}-\overline{y})}{\sqrt{\sum_{i=1}^{n}\sum_{j=1}^{m\text{-lag}}(x_{i,j}-\overline{x})^2\sum_{i=1}^{n}\sum_{j=1}^{m\text{-lag}}(y_{i,j+\text{lag}}-\overline{y})^2}}, \tag{A1}$$

where i is the index over the runs ($n = 100$), j is the index over the lags with m being the length the period that is considered to compute the correlation ($m = 155$ years for historical, $m = 50$ years for the ensemble with the strong CO_2 forcing. The term $\overline{x}$ is the time mean ensemble mean of x for the time steps 1 to m-lag, and $\overline{y}$ is the time mean ensemble mean of y for the time steps lag to m. Simply speaking, this means that we cut the last lag time steps of time series x from all ensemble members and created a new sample x' by concatenating all ensemble members so that $x' = (x_{1,1}, \ldots, x_{1,m\text{-lag}}, x_{2,1}, \ldots, x_{n,m\text{-lag}}, \ldots, x_{n,1}, \ldots x_{n,m\text{-lag}})$. The same was done for y, but with cutting the first lag time steps of every time series, so that $y' = (y_{1,\text{lag}}, \ldots, y_{1,m}, y_{2,\text{lag}}, \ldots, y_{n,m}, \ldots, y_{n,\text{lag}}, \ldots, y_{n,m})$. Our entire ensemble lag correlation is the correlation between x' and y'. For lag 0 this means that x' and y' have a length of 155 years × 100 runs = 15 500 time steps for the historical ensemble, respectively, 50 years × 100 runs = 5000 time steps for the ensemble with strong CO_2 forcing. The larger the lag, the fewer the number of data the correlation is based on. However, even for the largest lag that we show in this paper (which is 26 years), the correlations are based on 2400 time steps and our significance test shows that spurious correlation is very unlikely even in this case.

REFERENCES

Argo, 2000: Argo float data and metadata from the Global Data Assembly Centre (Argo GDAC). SEANOE, Accessed 27 February 2020, https://doi.org/10.17882/42182.

Ba, J., and Coauthors, 2014: A multi-model comparison of Atlantic multidecadal variability. *Climate Dyn.*, **43**, 2333–2348, https://doi.org/10.1007/s00382-014-2056-1.

Bellomo, K., L. N. Murphy, M. A. Cane, A. C. Clement, and L. M. Polvani, 2018: Historical forcings as main drivers of the Atlantic multidecadal variability in the CESM large ensemble. *Climate Dyn.*, **50**, 3687–3698, https://doi.org/10.1007/s00382-017-3834-3.

Booth, B. B. B., N. J. Dunstone, P. R. Halloran, T. Andrews, and N. Bellouin, 2012: Aerosols implicated as a prime driver of twentieth-century North Atlantic climate variability. *Nature*, **484**, 228–232, https://doi.org/10.1038/nature10946.

Boulton, C. A., L. C. Allison, and T. M. Lenton, 2014: Early warning signals of Atlantic meridional overturning circulation collapse in a fully coupled climate model. *Nat. Commun.*, **5**, 5752, https://doi.org/10.1038/ncomms6752.

Caesar, L., S. Rahmstorf, A. Robinson, G. Feulner, and V. Saba, 2018: Observed fingerprint of a weakening Atlantic Ocean overturning circulation. *Nature*, **556**, 191–196, https://doi.org/10.1038/s41586-018-0006-5.

Cane, M. A., A. C. Clement, L. N. Murphy, and K. Bellomo, 2017: Low-pass filtering, heat flux, and Atlantic multidecadal variability. *J. Climate*, **30**, 7529–7553, https://doi.org/10.1175/JCLI-D-16-0810.1.

Clement, A., K. Bellomo, L. N. Murphy, M. A. Cane, T. Mauritsen, G. Rädel, and B. Stevens, 2015: The Atlantic multidecadal oscillation without a role for ocean circulation. *Science*, **350**, 320–324, https://doi.org/10.1126/science.aab3980.

Delworth, T. L., and M. E. Mann, 2000: Observed and simulated multidecadal variability in the Northern Hemisphere. *Climate Dyn.*, **16**, 661–676, https://doi.org/10.1007/s003820000075.

——, F. Zeng, L. Zhang, R. Zhang, G. A. Vecchi, and X. Yang, 2017: The central role of ocean dynamics in connecting the North Atlantic Oscillation to the extratropical component of the Atlantic multidecadal oscillation. *J. Climate*, **30**, 3789–3805, https://doi.org/10.1175/JCLI-D-16-0358.1.

Drews, A., and R. J. Greatbatch, 2016: Atlantic multidecadal variability in a model with an improved North Atlantic current. *Geophys. Res. Lett.*, **43**, 8199–8206, https://doi.org/10.1002/2016GL069815.

——, and ——, 2017: Evolution of the Atlantic multidecadal variability in a model with an improved North Atlantic current. *J. Climate*, **30**, 5491–5512, https://doi.org/10.1175/JCLI-D-16-0790.1.

Drijfhout, S. S., S. L. Weber, and E. Swaluw, 2010: The stability of the MOC as diagnosed from model projections for pre-industrial, present and future climates. *Climate Dyn.*, **37**, 1575–1586, https://doi.org/10.1007/s00382-010-0930-z.

Eden, C., and T. Jung, 2001: North Atlantic interdecadal variability: Oceanic response to the North Atlantic Oscillation (1865–1997). *J. Climate*, **14**, 676–691, https://doi.org/10.1175/1520-0442(2001)014<0676:NAIVOR>2.0.CO;2.

Frankignoul, C., and K. Hasselmann, 1977: Stochastic climate models, Part II Application to sea-surface temperature anomalies and thermocline variability. *Tellus*, **29**, 289–305, https://doi.org/10.3402/tellusa.v29i4.11362.

Giorgetta, M. A., and Coauthors, 2013: Climate and carbon cycle changes from 1850 to 2100 in MPI-ESM simulations for the Coupled Model Intercomparison Project phase 5. *J. Adv. Model. Earth Syst.*, **5**, 572–597, https://doi.org/10.1002/jame.20038.

Gregory, J. M., and Coauthors, 2005: A model intercomparison of changes in the Atlantic thermohaline circulation in response to increasing atmospheric CO_2 concentration. *Geophys. Res. Lett.*, **32**, L12703, https://doi.org/10.1029/2005GL023209.

Gulev, S. K., M. Latif, N. Keenlyside, W. Park, and K. P. Koltermann, 2013: North Atlantic Ocean control on surface heat flux on multidecadal timescales. *Nature*, **499**, 464–467, https://doi.org/10.1038/nature12268.

Hasselmann, K., 1976: Stochastic climate models Part I. Theory. *Tellus*, **28**, 473–485, https://doi.org/10.3402/tellusa.v28i6.11316.

Hetzinger, S., M. Pfeiffer, W.-C. Dullo, N. Keenlyside, M. Latif, and J. Zinke, 2008: Caribbean coral tracks Atlantic multidecadal oscillation and past hurricane activity. *Geology*, **36**, 11–14, https://doi.org/10.1130/G24321A.1.

Hodson, D. L. R., J. I. Robson, and R. T. Sutton, 2014: An anatomy of the cooling of the North Atlantic Ocean in the 1960s and 1970s. *J. Climate*, **27**, 8229–8243, https://doi.org/10.1175/JCLI-D-14-00301.1.

IPCC, 2013: *Climate Change 2013: The Physical Science Basis*. Cambridge University Press, 1535 pp., https://doi.org/10.1017/CBO9781107415324.

Jungclaus, J. H., and Coauthors, 2013: Characteristics of the ocean simulations in the Max Planck Institute Ocean Model (MPIOM) the ocean component of the MPI-Earth System Model. *J. Adv. Model. Earth Syst.*, **5**, 422–446, https://doi.org/10.1002/jame.20023.

Kim, W. M., S. G. Yeager, and G. Danabasoglu, 2018: Key role of internal ocean dynamics in Atlantic multidecadal variability during the last half century. *Geophys. Res. Lett.*, **45**, 13 449–13 457, https://doi.org/10.1029/2018GL080474.

Latif, M., and Coauthors, 2004: Reconstructing, monitoring, and predicting multidecadal-scale changes in the North Atlantic thermohaline circulation with sea surface temperature. *J. Climate*, **17**, 1605–1614, https://doi.org/10.1175/1520-0442(2004)017<1605:RMAPMC>2.0.CO;2.

Li, F., M. S. Lozier, and W. E. Johns, 2017: Calculating the meridional volume, heat, and freshwater transports from an observing system in the subpolar North Atlantic: Observing system simulation experiment. *J. Atmos. Oceanic Technol.*, **34**, 1483–1500, https://doi.org/10.1175/JTECH-D-16-0247.1.

Lozier, M. S., V. Roussenov, M. S. C. Reed, and R. G. Williams, 2010: Opposing decadal changes for the North Atlantic meridional overturning circulation. *Nat. Geosci.*, **3**, 728–734, https://doi.org/10.1038/ngeo947.

Maher, N., and Coauthors, 2019: The Max Planck Institute Grand Ensemble: Enabling the exploration of climate system variability. *J. Adv. Model. Earth Syst.*, **11**, 2050–2069, https://doi.org/10.1029/2019MS001639.

Marsland, S. J., H. Haak, J. H. Jungclaus, M. Latif, and F. Röske, 2003: The Max-Planck-Institute global ocean/sea ice model with orthogonal curvilinear coordinates. *Ocean Modell.*, **5**, 91–127, https://doi.org/10.1016/S1463-5003(02)00015-X.

Murphy, L. N., K. Bellomo, M. Cane, and A. Clement, 2017: The role of historical forcings in simulating the observed Atlantic multidecadal oscillation. *Geophys. Res. Lett.*, **44**, 2472–2480, https://doi.org/10.1002/2016GL071337.

Oldenburg, D., K. C. Armour, L. Thompson, and C. M. Bitz, 2018: Distinct mechanisms of ocean heat transport into the Arctic under internal variability and climate change. *Geophys. Res. Lett.*, **45**, 7692–7700, https://doi.org/10.1029/2018GL078719.

O'Reilly, C. H., M. Huber, T. Woollings, and L. Zanna, 2016: The signature of low-frequency oceanic forcing in the Atlantic multidecadal oscillation. *Geophys. Res. Lett.*, **43**, 2810–2818, https://doi.org/10.1002/2016GL067925.

Otterå, O. H., M. Bentsen, H. Drange, and L. Suo, 2010: External forcing as a metronome for Atlantic multidecadal variability. *Nat. Geosci.*, **3**, 688–694, https://doi.org/10.1038/ngeo955.

Qasmi, S., C. Cassou, and J. Boé, 2017: Teleconnection between Atlantic multidecadal variability and European temperature: Diversity and evaluation of the Coupled Model Intercomparison Project phase 5 models. *Geophys. Res. Lett.*, **44**, 11 140–11 149, https://doi.org/10.1002/2017GL074886.

Rayner, N. A., D. E. Parker, E. B. Horton, C. K. Folland, L. V. Alexander, D. P. Rowell, E. C. Kent, and A. Kaplan, 2003: Global analyses of sea surface temperature, sea ice, and night marine air temperature since the late nineteenth century. *J. Geophys. Res.*, **108**, 4407, https://doi.org/10.1029/2002JD002670.

Reintges, A., T. Martin, M. Latif, and N. S. Keenlyside, 2017: Uncertainty in twenty-first century projections of the Atlantic meridional overturning circulation in CMIP3 and CMIP5 models. *Climate Dyn.*, **49**, 1495–1511, https://doi.org/10.1007/s00382-016-3180-x.

Schlesinger, M. E., and N. Ramankutty, 1994: An oscillation in the global climate system of period 6570 years. *Nature*, **367**, 723–726, https://doi.org/10.1038/367723a0.

Smeed, D. A., and Coauthors, 2014: Observed decline of the Atlantic meridional overturning circulation 2004–2012. *Ocean Sci.*, **10**, 29–38, https://doi.org/10.5194/os-10-29-2014.

Stevens, B., and Coauthors, 2013: Atmospheric component of the MPI-M Earth System Model: ECHAM6. *J. Adv. Model. Earth Syst.*, **5**, 146–172, https://doi.org/10.1002/jame.20015.

Svendsen, L., S. Hetzinger, N. Keenlyside, and Y. Gao, 2014: Marine-based multiproxy reconstruction of Atlantic multidecadal variability. *Geophys. Res. Lett.*, **41**, 1295–1300, https://doi.org/10.1002/2013GL059076.

Tandon, N. F., and P. J. Kushner, 2015: Does external forcing interfere with the AMOCs influence on North Atlantic sea surface temperature? *J. Climate*, **28**, 6309–6323, https://doi.org/10.1175/JCLI-D-14-00664.1.

Terray, L., 2012: Evidence for multiple drivers of North Atlantic multi-decadal climate variability. *Geophys. Res. Lett.*, **39**, L19712, https://doi.org/10.1029/2012GL053046.

Yan, X., R. Zhang, and T. R. Knutson, 2018: Underestimated AMOC variability and implications for AMV and predictability in CMIP models. *Geophys. Res. Lett.*, **45**, 4319–4328, https://doi.org/10.1029/2018GL077378.

Yeager, S., 2015: Topographic coupling of the Atlantic overturning and gyre circulations. *J. Phys. Oceanogr.*, **45**, 1258–1284, https://doi.org/10.1175/JPO-D-14-0100.1.

Zhang, J., and R. Zhang, 2015: On the evolution of Atlantic meridional overturning circulation fingerprint and implications for decadal predictability in the North Atlantic. *Geophys. Res. Lett.*, **42**, 5419–5426, https://doi.org/10.1002/2015GL064596.

Zhang, R., R. Sutton, G. Danabasoglu, T. L. Delworth, W. M. Kim, J. Robson, and S. G. Yeager, 2016: Comment on "The Atlantic multidecadal oscillation without a role for ocean circulation." *Science*, **352**, 1527, https://doi.org/10.1126/science.aaf1660.